Band-Gap Reduction in (BiCrO_{3})_{m}/(BiFeO_{3})_{n} Superlattices: Designing Low-Band-Gap Ferroelectrics

S. Zhang, H.Y. Xiao, S.M. Peng, G.X. Yang, Z.J. Liu, X.T. Zu, S. Li, D.J. Singh, L.W. Martin, and L. Qiao

Phys. Rev. Applied **10**, 044004 — Published 2 October 2018

DOI: 10.1103/PhysRevApplied.10.044004

Band-Gap Reduction in $(BiCrO_3)_m/(BiFeO_3)_n$ Superlattices: Designing New Low-Band-Gap Ferroelectrics

S. Zhang[a], H.Y. Xiao,[a,*] S. M. Peng[b], G. X. Yang[b], Z. J. Liu,[c] X.T. Zu[a], S. Li,[d] D. J. Singh,[e] L. W Martin,[f,g] and L. Qiao[a,d*]

[a] *School of Physics, University of Electronic Science and Technology of China, Chengdu 610054, China*

[b] *Institute of Nuclear Physics and Chemistry, Chinese Academy of Engineering Physics, Mianyang 621900, China*

[c] *Department of Physics, Physics, Lanzhou City University, Lanzhou 730070, China*

[d] *School of Materials, University of New South Wales, Sydney, AU*

[e] *Department of Physics and Astronomy, University of Missouri, Columbia, Missouri 65211-7010, USA*

[f] *Department of Materials Science and Engineering, University of California, Berkeley, Berkeley, CA 94720 USA*

[g] *Materials Sciences Division, Lawrence Berkeley National Laboratory, Berkeley, CA 94720 USA*

Abstract：

Ferroelectric $BiFeO_3$ is promising for photovoltaic applications, especially in regard to the exploitation of ferroelectric photovoltaic effects for charge separation. However, its large band gap limits efficient sunlight absorption. Here, we demonstrate a new strategy to effectively tune the band gap of tetragonal $BiFeO_3$ via superlattice

structuring with the ferroelectric $BiCrO_3$. The $(BiCrO_3)_m/(BiFeO_3)_n$ superlattices are found to exhibit conventional ferroelectric properties, but low fundamental band gaps, smaller than either of the parent materials. First-principles calculations reveal that the unexpected band-gap reduction is induced by charge reconstruction due to lattice strain, octahedral distortion, and polarization discontinuity at the $BiCrO_3$ - $BiFeO_3$ interfaces. Ultimately, these results provide a new strategy, in the form of superlattice structuring, which could open the door to the creation of efficient ferroelectric photovoltaics.

Keywords: Band gap tuning; $BiFeO_3$; Superlattice; Density functional theory;

* Corresponding author. E-mail address:

hyxiao@uestc.edu.cn (H.Y. Xiao)

liang.qiao@uestc.edu.cn (L. Qiao)

I. INTRODUCTION

In the past several decades, researchers have been striving to open different corridors for the production of renewable energy. In this regard, photovoltaics (PVs) have been demonstrated to be a promising renewable energy technology to harvest solar energy [1-3], one of the most abundant energy sources available on Earth[4]. Generally, the performance of PV materials is quantified by the power conversion efficiency (PCE), which can be related to the photovoltage and photocurrent. Recently, building from initial interest in single-crystal and ceramic materials over four decades ago [5], a rejuvenation of interest in the so-called anomalous photovoltaic effect in non-centrosymmetric thin-film ferroelectrics has driven an urgent search for new materials in this space. Contrary to traditional semiconductor-based PVs, the photovoltage of ferroelectrics is not limited by their band gap, but can be a few orders of magnitude larger than the optical band gap of material itself [5,6]. In some cases, the photovoltage has been found to be $> 10^4$ V [2,6]. Generally the photovoltage is proportional to the magnitude of the electric polarization [6-9]; however, the PCE of ferroelectric materials is normally limited by their small photocurrent density, typically on the order of nA/cm^2, which mainly originates from the large intrinsic band gap of these materials (typically 3-4 eV) [2,10]. It is, therefore, of significant importance to lower the band gap of ferroelectric materials without affecting the ferroelectric polarization in an attempt to improve the PCE in PV applications. This is also of great importance for fully characterizing ferroelectric photovoltaic effects, including understanding the performance limits of these devices. While ferroelectric

semiconductors do exist [11], for reasons yet to be understood, the largest effects have been observed in oxides, and therefore finding better oxide materials is a key challenge in the field.

A focus has been in $BiFeO_3$ due to its intrinsic, relatively low band gap (2.67-3.1 eV) [12] and high polarization (90-158 μC/cm^2) [13-15]. Importantly, the $BiFeO_3$ has been widely investigated for PV applications and so far shows better PCE efficiency than most of other ferroelectric materials [2,16-20], making it a highly desirable ingredient in fabricating new ferroelectric photovoltaics. Despite these successes, however, $BiFeO_3$ can only absorb UV light, which constitutes only ~20 % of the entire solar spectrum; leaving most of the solar energy incident on Earth unexploited [21]. In epitaxial $BiFeO_3$ thin films, there are several possible phases, including structures derived from monoclinic, triclinic, orthorhombic, and tetragonal parent structures. Of particular note is the tetragonal-like phase, which is actually a slightly monoclinically-distorted tetragonal structure, and has a large *c*/*a* lattice parameter ratio of ~1.26 and a giant spontaneous polarization approaching ~150 μC/cm^2. ***With this in mind, it is meaningful to reduce the band gap of tetragonal-like $BiFeO_3$, while maintaining the large spontaneous polarization, to enhance the PCE***. On the other hand, $BiCrO_3$ is another ferroelectric material, also with an active lone-pair on the bismuth cation [22], which is often used to tune the band gap and photocurrent of $BiFeO_3$ [23-26], e.g. through alloying. We have recently studied alloyed $BiCrO_3$-$BiFeO_3$ films and found that chromium substitution can help to reduce the band gap by ~0.8 eV for solid solution films and improves charge transport [27]. The

$BiCrO_3/BiFeO_3$ bilayer films, synthesized using a sol-gel technique, were found to exhibit a band gap of ~2.25 eV (smaller than the value of 2.64 eV of $BiFeO_3$) and a short circuit photocurrent density of 0.08 mA/cm^2 (higher than the value of 0.007 mA/cm^2 for a single-layer $BiFeO_3$ film) [28]. Multiferroic $BiFeO_3/BiCrO_3$ heterostructures have also been studied experimentally [10], and it was reported that the photocurrent density and photovoltage can be tuned by the thickness and the number of $BiFeO_3/BiCrO_3$ bilayers and that the highest photocurrent density value (~0.013 mA/cm^2) was recorded in 60-nm-thick heterostructures (including two $BiFeO_3/BiCrO_3$ bilayers with each layer of thickness of 15 nm).

More recently, significant band-gap reduction has been realized in double-perovskite Bi_2CrFeO_6, in which *B*-site-cation ordering controlled by film synthesis results in a remarkable PCE over 8.1 % under AM 1.5G irradiation [21]; a new record for inorganic perovskites in conventional solar-cell applications. The mechanism of enhanced visible-light absorption and its correlation with cation ordering in the double-perovskite Bi_2CrFeO_6, however, is not clear. It is well known that for perovskites, achieving *B*-site-cation ordering is very difficult (and it is particularly sensitive to oxygen partial pressure and growth temperature) as the thermodynamic window allowing for the realization of such ordered states is extremely narrow. This has been shown true in a number of systems, including La_2VMnO_6 [29], La_2CrFeO_6 [30], and La_2NiMnO_6 [31], etc. ***On the other hand, superlattice ordering is also a powerful method to engineer ordered double-perovskite structures. For example, long-range ferromagnetism has been***

reported in $LaCrO_3$/$LaFeO_3$ superlattices, which is unexpected, given that both $LaCrO_3$ and $LaFeO_3$ are antiferromagnetic [32]. Therefore, by creating an atomically-ordered state via superlattice structuring of the aforementioned $BiFeO_3$ and $BiCrO_3$, one might expect to yield interesting electronic structure and material properties, distinct from alloys. There has been limited studies on $BiCrO_3$/$BiFeO_3$ superlattices, and those which do exists have focused mainly on traditional ferroelectric behavior. For example, using a scanning non-linear dielectric microscope, researchers found that the polarization in such superlattices is reversible and thus suggested that the superlattices are ferroelectric at room temperature [33]. The ground state properties of $BiFeO_3$/$BiCrO_3$ superlattices, such as the electronic structure, intrinsic band gap, and ferroelectric polarization, are, however, not well developed.

Here, we report a density functional theory (DFT) investigation of the lattice geometrical and electronic properties of $(BiCrO_3)_m$/$(BiFeO_3)_n$ superlattices. Systematic study shows that the band gap of the superlattices is widely tunable, and can take values well below those of either component by itself, while still maintaining the ferroelectric polarization. Unexpectedly, the optimized band gap of ~1.6 eV for the $BiCrO_3$/$BiFeO_3$ superlattice is not only smaller than both the single-layer $BiFeO_3$ and $BiCrO_3$, but is also smaller than the equivalent $Bi(Fe,Cr)O_3$ alloy [27]. This surprising result is the consequence of charge reconstruction due to lattice strain, octahedral distortion, and polarization discontinuity at the superlattice interfaces. We also show that the ferroelectric and magnetic properties of the superlattice are not strongly affected. These results demonstrate that superlattice structuring can be an

effective strategy for the design of low band gap oxide semiconductors with fundamental band gaps much smaller than either parent materials, thus opening new perspectives for ferroelectric PVs.

II. COMPUTATIONAL DETAILS

All of the spin-polarized calculations are carried out based on the DFT, using the Vienna ab-initio Simulation Package (VASP) code [34,35]. For the exchange and correlation energy, the Perdew-Burke-Ernzerhof functional [36] under the generalized gradient approximation (GGA) is employed. The on-site Coulomb interaction presented in 3*d* states of transition-metal ions are corrected by the DFT+U (where U is the Hubbard energy) method [37]. The dependence of the lattice parameters and band gap for $BiFeO_3$ on the effective U value are presented [Fig. 1(a) and (c)]. It is shown that as the U_{eff} value increases, the lattice parameter *a* and *c/a* deviate from and approach to the experimental values, respectively. On the other hand, the band gap increases till U_{eff}=3 eV and further increase has slight influence on the band gap. For $BiCrO_3$, similar trend is observed. Consequently, the U_{eff}=4 eV [27,38] is employed for both Fe 3*d* and Cr 3*d* states in this work. A cutoff energy of 500 eV for plane-wave basis set and a 4×4×4 Monkhorst-Pack k-mesh for Brillouin-zone integrations are used for structural relaxation. The convergence criteria for total energies and forces are 10^{-4} eV and 10^{-4} eV/Å, respectively. During the structural optimization, a full relaxation is employed. The spontaneous polarization is evaluated by simply summing the product of atomic displacements and corresponding Born effective charges (BECs)

[39], which are calculated using density functional perturbation theory with a 2×2×2 Monkhorst-Pack k-mesh. ***For bulk $BiFeO_3$ (BFO) and $BiCrO_3$ (BCO), all computations are based on a 2×2×2 supercell containing 40 atoms. For the $(BiCrO_3)_m/(BiFeO_3)_n$ $((BCO)_m/(BFO)_n)$ superlattices,*** which consist of m unit cells of $BiCrO_3$ alternating with n unit cells of $BiFeO_3$, different alternating periodic cells, *i.e.*, $(BCO)_m/(BFO)_1$ and $(BCO)_1/(BFO)_n$ (m, n = 1, 2, 3, 4, 5), are considered.

III. RESULTS AND DISCUSSION

A. Ground state properties of bulk BFO and BCO

The tetragonal-like phase of BFO with a space group of *P*4*mm* has a large *c/a* lattice parameter ratio (1.255-1.27) [12,40], where O_A and O_B, respectively, belong to the FeO and BiO layers [Fig. 2 (a)]. Clearly, one Fe^{3+} is coordinated by six O^{2-} ions and an octahedron is formed. In the literature, it has been reported that the tetragonal-like BFO has G- and C-type antiferromagnetic spin states [38,41]. Schematic views of the spin configurations of BFO are illustrated [Fig. 2(b)-(c)]; in this work, both G- and C-type ordering are considered for bulk BFO and BCO.

For bulk BFO, the obtained lattice parameters of a = 3.755 Å and c/a = 1.300 for G-type ordering are close to the calculated values of 3.753 Å and 1.303, respectively, for C-type ordering; both are in good agreement with the experimental values of 3.72 Å and 1.255 [40], respectively. The calculated magnetic moment of Fe is 4.136 μ_B/atom for G-type ordering, agreeing well with the prior theoretical value of 4.18 μ_B/atom [42] and the experimental value of 4.34 μ_B/atom [43], and it is comparable to

the result of 4.130 μ_B/atom for C-type ordering. Both G- and C-type ordered BFO exhibit direct band gaps and the values of band gap are 1.62 and 1.71 eV, respectively; which are smaller than the experimental data of 3.1 eV [12,44,45]. This is a generic problem in DFT, which persists in the PBE+U calculations, with U=4 eV. Higher values of U have slight effects on the band gap, and ***so we use U=4 eV, and correct the band gap using a scissors operation [46,47] based on the known experimental gap of $BiFeO_3$ and $BiCrO_3$ (see the part C of section III)***. Our calculations show that the geometrical structure, band structure and Fe magnetic moment of G- and C-type ordered tetragonal BFO are similar to each other, which is consistent with previous theoretical studies [38]. We also find that the total energy difference between G- and C-type ordered BFO is only 0.068 eV, indicating that the stability of these two orderings are comparable.

For bulk G- and C-type ordered BCO, the obtained magnetic moment of Cr and the lattice parameters are, like for the case of BFO, similar to each other [Table 1]. For G-type ordered BCO, the calculated lattice parameters are a = 3.926 Å and c = 4.073 Å, which are comparable to the experimental results of a = 3.888 Å and c = 3.902 Å [48]. On the other hand, the band gap of 0.94 eV for G-type ordering is higher than the value of 0.69 eV for C-type ordering, and both values are smaller than the experimental value of 2.37 eV [28]. ***The calculated band gap of BCO (0.94 eV for G-type and 0.69 eV for C-type) are smaller than those of BFO (1.62 eV for G-type and 1.71 eV for C-type), consistent with the experimental results.*** [12,28]. In addition, the total energy of the G-type ordering is 0.156 eV smaller than C-type

ordering, *i.e.*, the G-type ordering BCO is energetically more preferable. Hence, in the subsequent calculations, we only consider the BFO and BCO with G-type ordering.

B. Geometrical structures of the superlattices

Fig. 2(d) illustrates the geometrical structure for the optimized $(BCO)_1/(BFO)_1$ superlattice. The optimized structural parameters of $(BCO)_m/(BFO)_1$ and $(BCO)_1/(BFO)_n$ superlattices are also presented [Table 2], including data for bulk BFO and BCO. The calculated lattice constant *a* and average *c*/*a* ratio as a function of m and n are also plotted [Fig. 3 (a)]. It is found that the in-plane lattice constant *a* of $(BCO)_m/(BFO)_1$ increases with increasing BCO layers, and the in-plane lattice constant of $(BCO)_1/(BFO)_n$ decreases with increasing BFO layers, owing to the strain effect caused by the lattice mismatch between BFO and BCO. To the contrary, as can be seen [Fig. 3(b)], the average out-of-plane lattice constant *c* of the superlattices decreases with increasing BCO layers and increases with increasing BFO layers. For displacive ferroelectric materials, the *c*/*a* ratio reflects the tetragonal distortion, which is a consequence of the spontaneous polarization. Therefore, the observed increase of *c*/*a* ratio indicates an increase of relative displacement between cations and anions, resulting in enhanced polarization [49,50]. The *c*/*a* ratio decreases with increasing BCO layers and increases with increasing BFO layers [Fig. 3(b)], indicating that the polarization of the $(BCO)_1/(BFO)_n$ superlattices is larger than that of the $(BCO)_m/(BFO)_1$ superlattices. This is seen directly in the polarization discussed in the next section. It is thus expected that the electrical and optical properties of the

$(BCO)_m/(BFO)_n$ superlattices can be adjusted by tuning the stacking period, which will alter the ground-state structure of superlattices due to strain effects [50].

The average interlayer distance Δd (the thickness of one monolayer, which is equivalent to the local out-of-plane lattice constant) and the bond angles $\angle O_A\text{-}Cr\text{-}O_B$ and $\angle O_A\text{-}Fe\text{-}O_B$ in BFO, BCO and the $(BCO)_m/(BFO)_n$ superlattices are also summarized [Table 2]. We find that all the values of Δd_{BFO} for superlattices are smaller than the value of 4.879 Å for bulk BFO and the values of Δd_{BCO} are larger than the value of 4.073 Å for bulk BCO, indicating that the BFO in the $(BCO)_1/(BFO)_n$ superlattices is compressed, while the BCO in the $(BCO)_m/(BFO)_1$ superlattices is stretched along the [001] direction in comparison to their bulk values. This is resulted from the interface stress caused by the large lattice mismatch (4.3 %) between the BFO and BCO, since the lattice constant of BFO (3.755 Å) is much smaller than that of BCO (3.926 Å). For the $(BCO)_m/(BFO)_1$ superlattices, as the number of BCO layers increases from 1 to 5, Δd_{BFO} decreases from 4.456 to 4.166 Å, and Δd_{BCO} decreases from 4.327 to 4.094 Å. Obviously, for the thicker BCO layers, the interlayer spacing of BFO is far from that in the bulk state and the interlayer distance between BCO layers becomes close to that in the bulk. Correspondingly, the $\angle O_A\text{-}Fe\text{-}O_B$ angle deviates much more from the 110.7° in the bulk state and the $\angle O_A\text{-}Cr\text{-}O_B$ angle approaches the 96.6° in the bulk state. These results suggest that the thicker BCO layers lead to significant compression of the BFO and large relaxation of BCO layers along the [001] direction. As for the $(BCO)_1/(BFO)_n$ superlattices, when the BFO layer is increased in thickness from 1 to 5 unit cells, the BFO layer is

compressed and the BCO layer is expanded considerably, resulting in Δd_{BFO} and $\angle O_A\text{-Fe-}O_B$ approaching the bulk values for BFO and Δd_{BCO} and $\angle O_A\text{-Cr-}O_B$ deviating significantly from the bulk values for BCO. Comparing the bond angles $\angle O_A\text{-Cr-}O_B$ and $\angle O_A\text{-Fe-}O_B$ in both the $(BCO)_1/(BFO)_n$ and $(BCO)_m/(BFO)_1$ superlattices, we find that both angles in the $(BCO)_1/(BFO)_n$ superlattices are larger than those in the $(BCO)_m/(BFO)_1$ superlattices, indicating that the distortion of the octahedra in the tetragonal lattice of the $(BCO)_1/(BFO)_n$ superlattices is more significant, which results in larger *c*/*a* ratio and polarization [49]. This is in good agreement with the discussions in above section. It is obvious that the induced structural deformation and octahedral distortion in the $(BCO)_1/(BFO)_n$ and $(BCO)_m/(BFO)_1$ superlattices are different, indicating that they may exhibit different electronic structures and polarization.

The formation of these superlattices can be quantitatively estimated by their respective formation energy, which reflects the total energy cost during the superlattice structuring of the two parent compounds BFO and BCO. The formation energies of $(BCO)_m/(BFO)_n$ superlattices as compared to bulk BFO and BCO are calculated and the results are summarized [Table 3]. The formation energy is defined as $E=E_{(BCO)m/(BFO)n}-nE_{bulkBFO}-mE_{bulkBCO}$. Here, $E_{(BCO)m/(BFO)n}$, $E_{bulkBFO}$ and $E_{bulkBCO}$ are the total energies of $(BCO)_m/(BFO)_n$ superlattices, bulk BFO and bulk BCO, respectively. As shown in Table 3, the $(BCO)_1/(BFO)_1$ superlattice has the lowest formation energy of 1.94 eV among the considered superlattices, and the formation energies of $(BCO)_m/(BFO)_1$ and $(BCO)_1/(BFO)_n$ superlattices increase with the

increasing layer number of BCO and BFO, respectively. It is also noted that the formation energy of $(BCO)_m/(BFO)_1$ is relatively smaller than that of $(BCO)_1/(BFO)_n$ (m=n=2, 3, 4, 5). These results suggest that as the layer number of BFO or BCO is increased the $(BCO)_m/(BFO)_1$ and $(BCO)_1/(BFO)_n$ superlattices become more difficult to form, and the $(BCO)_1/(BFO)_n$ superlattices are relatively more difficult to form than the $(BCO)_m/(BFO)_1$ superlattices.

In order to investigate if the superlattice structures are mechanically stable, we select the $(BCO)_1/(BFO)_1$ superlattice as a model system and calculate its elastic constants. The obtained elastic constants are C_{11} of 260.1 GPa, C_{33} of 64.4 GPa, C_{44} of 79.1 GPa, C_{66} of 59.4 GPa, C_{12} of 75.3 GPa and C_{13} of 78.3 GPa, which satisfy well the Born stability criteria, i.e., $C_{11} > 0$, $C_{33} > 0$, $C_{44} > 0$, $C_{66} > 0$, $(C_{11}- C_{12}) > 0$, $(C_{11}+C_{33}-2C_{13}) > 0$, $[2(C_{11}+C_{12})+C_{33}+4C_{13}] > 0$, indicating that the $(BCO)_1/(BFO)_1$ superlattice is mechanically stable. The lattice mismatch between bulk BFO and BCO is about 4.3 %. Experimentally, the $LaAlO_3/BaTiO_3$, $PbTiO_3/PbZrO_3$, and $BaZrO_3/SrTiO_3$ superlattices, for which the lattice mismatch are 5.3 %, 5.3 % and 6.9 %, respectively, have been synthesized successfully by Zuo et. al. [51], Choi et. al. [52] and Christen et. al. [53], respectively. Hence, the BFO/BCO superlattice, with a lattice mismatch of ~ 4.3 %, is possible to be synthesized with an appropriate substrate. Recently, the supertetragonal phase of BFO has been successfully synthesized by various groups via epitaxial stabilization on $LaAlO_3$ and $YAlO_3$ with pulsed laser deposition method [54-57]. Considering suitable lattice match for both BFO and BCO, we propose $LaAlO_3$ can be a very good candidate for the

experimental realization of the BCO/BFO superlattice with tetragonal phase.

C. Electronic structures of the superlattices

Based on the optimized structures, we further calculate the band structures of the $(BCO)_m/(BFO)_1$ and $(BCO)_1/(BFO)_n$ superlattices. In this study, an approach of reverse scissor correction procedure is employed. This is an empirical correction consisting of a shift of the conduction regions up and can be applied to both GGA and LDA underestimated band gaps, especially in the determination of band-gap offsets for interfaces between different semiconductors [46,58,59]. The scissor correction method has been extensively employed in a number of calculations and the predicted band gap and optical properties were found to agree well with experiments. [47,60-62]. ***Here we use a scissor operator of 1.48 eV, which corrects not only the band gap of BFO to 3.1 eV but also the band gap of BCO to 2.42 eV,*** agreeing well with the experimental values of 3.1 eV [12,45] and 2.37 eV [28], respectively. The scissor operator of 1.48 eV is also applied to the $(BCO)_m/(BFO)_n$ superlattice structure.

The variation of the reverse scissor corrected band gap for $(BCO)_1/(BFO)_n$ and $(BCO)_m/(BFO)_1$ superlattices as a function of the number of BFO and BCO layers [Fig. 4(a)] and the calculated band structures [Fig. 5] are presented. It is shown that all the superlattices retain the direct band gap character, similar with that of BFO. Besides, based on the calculated results, it appears that the charge hybridization and carrier transport will mainly occur within the tetragonal plane rather than along the *c*

axis, since the dispersion occurs along the G-X, X-M and M-G directions while the bands are flat along the G-Z direction [63]. The band gap of the superlattices is observed to decrease markedly with the number of layers of BFO and/or BCO in a given stack height [Fig. 4(a)]. The band gap of the $(BCO)_1/(BFO)_n$ superlattices are lower than that of the $(BCO)_m/(BFO)_1$ superlattices for the same values of n and m (n, m>1). The band-gap values for the superlattices are located within the range of 1.59-1.96 eV, which are unexpectedly smaller than the parent materials.

In order to verify if the scissor correction results for the superlattice structure are reliable, a series of DFT/meta-GGA calculations with mBJ (modified-Becke-Johnson) functional are also carried out. The DFT/meta-GGA method with mBJ functional (DFT/meta-GGA-mBJ) has been reported to yield band gaps with an accuracy similar to hybrid functional or GW methods for various semiconductors/insulators but computationally less expensive [64]. We have performed DFT/meta-GGA-mBJ calculations on BFO, BCO and $(BCO)_m/(BFO)_1$ (m=1 to 5) superlattices and a comparison of the obtained band gap by DFT, DFT with scissor correction and DFT/meta-GGA-mBJ calculations is listed in Table 4. For bulk BFO and BCO under DFT/meta-GGA-mBJ scheme, the weight parameters (cmBJ values) of 1.4 and 1.3 are employed, respectively, and the obtained band gap of 2.92 eV for bulk BFO and 2.27 eV for bulk BCO are in good agreement with the experimental values of 3.1 [12,45] and 2.37 eV [28], respectively. These cmBJ values are then applied to the $(BCO)_m/(BFO)_1$ (m=1 to 5) superlattices. It is noticeable that the band gap values predicted by scissor corrections compare well with those obtained from

DFT/meta-GGA-mBJ and both methods predict similar band gap variation trend, confirming the reliability of the current predicted band gap values.

Furthermore, the obtained value (1.59 -1.96 eV) is also substantially smaller than that of the alloyed $Bi(Fe,Cr)O_3$ sample [27]. Similar results wherein the band gap of a composite compound is smaller than that of the parent materials have also been reported in superlattices of $(GaN)_1/(ZnO)_1$ [65] and (0001)-oriented wurtzite $(GaN)_n/(AlN)_n$ (n = 10, 12, 14) [66] as well as nanocomposites of Carbon-ZrO_2 [67] , NiO:TiO_2 [68] and Fe_2O_3-Cr_2O_3 systems [69-71].

For the band gap reduction with the increasing layer number of BFO or BCO, the lattice strain induced by the lattice mismatch between BFO and BCO may be one of the reasons responsible for that. In order to explore how the lattice strain influences the band gap, we investigate the band gap of BFO and BCO within 2 % tensile and compressive strain, respectively. The variation of band gap as a function of strain is illustrated [Fig. 4(b)]. It is shown that the band gap of both BFO and BCO decreases monotonously with decreasing the compressive strain and increasing the tensile strain level. This predicted trend is consistent with recent experimental observation that film epitaxially grown on compressive substrate (e.g. $LaAlO_3$ and $YAlO_3$) exhibits relatively larger optical band gap than on tensile substrate (e.g. $DyScO_3$) [44,45,72,73].

For $(BCO)_m/(BFO)_1$ superlattices, the interlayer distances between BCO layers are comparable to that of bulk BCO and the interlayer distances between BFO layer are much smaller than that of bulk BFO, i.e., the tensile strain of BFO dominates in

the $(BCO)_m/(BFO)_1$ superlattices and the tensile strain increases with the increasing layer number of BCO. As for $(BCO)_1/(BFO)_n$ superlattices, the interlayer distances between BFO layers are comparable to that of bulk BFO and the interlayer distances between BCO layer are much larger than that of bulk BCO, i.e., the compressive strain of BCO dominates in the $(BCO)_1/(BFO)_n$ superlattices and the compressive strain increases with the increasing layer number of BFO.

It should be pointed out that the $(BCO)_m/(BFO)_n$ superlattice cannot be free-standing experimentally and a suitable substrate is necessary. Considering the error between calculated values and experimental measurements, the in-plane lattice constants of (BCO)/(BFO) superlattices would vary from 3.738 to 3.885 Å. Therefore, the $LaAlO_3$ (LAO), with a lattice constant of 3.79 Å, will be a suitable substrate for the synthesis of BFO/BCO superlattice. The lattice mismatch between the substrate and the superlattice structure is estimated to be 1.3~2.5 % and the induced lattice strain varies from -2.4 % to 1.4 %. We also study the strain effect on the band gap of the superlattice. The representative results of $(BCO)_1/(BFO)_1$ and $(BCO)_1/(BFO)_5$ are also shown in Fig. 4(b). It is clearly seen that the superlattice demonstrates similar trend of strain dependent band gap as single phase of BFO and BCO. However, the band gap variation is much smaller, for example, the band gap of $(BCO)_1/(BFO)_1$ superlattice change from 2.06 to 1.94 eV corresponding to -2% compressive strain to 2% tensile. Therefore, the epitaxial strain is not expected to significantly impact the band gap values of the superlattice systems.

In order to understand the origin of the unexpected band-gap reduction, further

electronic structure calculations are necessary. The partial charge density distributions at the valence-band maxima (VBM) and conduction-band minima (CBM) for BFO, BCO and the $(BCO)_1/(BFO)_5$ and $(BCO)_5/(BFO)_1$ superlattices are illustrated [Fig. 6]. It is found that holes at the VBM for BFO are mainly contributed by two types of oxygen anions, while the electrons at the CBM are mainly located on the A-site Bi and O_A atoms, respectively, and also slightly on the B-site Fe atom. For the BCO, the charge density distribution is remarkably different, the holes at the VBM are mainly gathered on the two types of O atoms as well as on B-site Cr atoms, while the electrons at the CBM are mainly contributed by the A-site Bi and O_A atoms, respectively. The different valence/conduction band characteristics of these two compounds originate from the different electron negativity of the transition-metal cations and thus the different electronic structures of BFO and BCO. The valence bands of BFO are mainly contributed by O 2*p* orbitals, whereas the O 2*p* and Cr 3*d* states dominate the valance bands of BCO in the band edge near the Fermi level [Fig. 7] due to the slight higher atomic energy position for Cr 3*d* orbitals than Fe 3*d* orbitals. ***These results indicate that electron redistribution should be expected when the BFO and BCO are incorporated simultaneously in the same superlattice structures***. Comparing the charge distribution of the $(BCO)_1/(BFO)_5$ superlattice with that of bulk BFO and BCO, we find that the holes at the VBM for the $(BCO)_1/(BFO)_5$ superlattices are mainly contributed by the interfacial Cr 3*d* and O 2*p* orbitals, and the electrons at the CBM are mainly gathered on the interfacial Fe 3*d*, Bi 6*p*, and a few O_A 2*p* orbitals. For the $(BCO)_5/(BFO)_1$ superlattices, the charge distribution of the

VBM and the CBM are similar to the $(BCO)_1/(BFO)_5$ superlattices, where the holes at the VBM are mainly contributed by the Cr and O_B ions and the electrons at the CBM are mainly gathered on the Bi and O_A ions. The atomic projected density of state distribution for bulk BFO, bulk BCO, $(BCO)_1/(BFO)_n$ and $(BCO)_n/(BFO)_1$ (n, m=1, 3, 5) superlattices is illustrated [Fig. 7]. It is noted that ***the Fermi level of the BFO is shifted to higher binding energy when the superlattice structure is formed, accompanied by the upward shift of the valence bands***. As compared with the DOS distribution of $(BCO)_1/(BFO)_1$ superlattice, it is noted that the Fermi levels shift slightly to the higher binding energy level and lower binding energy level for $(BCO)_1/(BFO)_n$ and $(BCO)_m/(BFO)_1$ superlattices, respectively. As for $(BCO)_1/(BFO)_n$ superlattices, the valence bands are mainly contributed by O 2*p* and Fe 3*d* states; in the case of $(BCO)_m/(BFO)_1$ superlattices, the O 2*p* and Cr 3*d* states dominate the valence bands. Also, the conduction bands of $(BCO)_1/(BFO)_n$ and $(BCO)_m/(BFO)_1$ superlattices exhibit different character. For the $(BCO)_1/(BFO)_n$ superlattices, the conduction bands shift towards Fermi level. Consequently, the band gap of the $(BCO)_1/(BFO)_n$ and $(BCO)_m/(BFO)_1$ superlattices is much lower than that of BFO.

D. Spontaneous polarization

An excellent ferroelectric PV material should have not only a low band gap and high photocurrent, but also a large spontaneous polarization. The polarization can be estimated by $\Delta P_\alpha \cong \sum_{j\beta} \frac{\partial P_\alpha}{\partial \mu_{j\beta}} \left(\mu_{j\beta} - \mu_{0j\beta}\right) = \frac{e}{\Omega} \sum_{j\beta} Z^*_{j\alpha\beta}\, \Delta\mu_{j\beta}$, where $\Delta\mu_{j\beta}$ is the

displacement of ions j in Cartesian direction β, $Z^*_{j\alpha\beta}$ is the Born effective charge tensor, e is the charge of an electron and the Ω is the cell volume [39]. In this work, cubic BFO is used as the centrosymmetric reference structure, which is described by the zero subscript. The calculated polarization for the tetragonal-like BFO by this method is 142.3 μC/cm^2; agreeing well with the experimental data of 150−158μC/cm^2 [13,40] and other prior calculated values of 136−145 μC/cm^2 [57,74,75]. The polarization as a function of BFO and BCO layer number is plotted [Fig. 8]. It is shown that the polarization of all superlattices are located in the range of 64.8-131.0 μC/cm^2. The polarization of the superlattices decreases with the increasing number of BCO layers, but increases with the increasing BFO layers, which is similar to the variation of the *c*/*a* ratio with layer number of both BFO and BCO. A similar dependence has been reported in tetragonal $(BaZrO_3)_m/(BaTiO_3)_n$ superlattices that have a large *c*/*a* ratio and large polarization [50]. We find that the polarization of the superlattices are mainly contributed by the transition elements and the O^{2-} ions, and the contribution of O_A is larger than that of O_B. Besides, the direction of polarization of transition elements is in opposition to that of O and Bi atoms. In addition, the polarization of 92.9-131.0 μC/cm^2 for the $(BCO)_1/(BFO)_n$ superlattices is larger than the polarization of 64.8-92.9 μC/cm^2 for the $(BCO)_m/(BFO)_1$ superlattices, and the value of 131.0 μC/cm^2 for the $(BCO)_1/(BFO)_5$ superlattices is the largest among all the investigated superlattices. This likely arises from the combined effects of lattice strain in the BFO layers due to lattice mismatch and the distorted octahedra in both the BFO and BCO.

In this study, a DFT+U method is employed to investigate the band gap and polarization of $(BCO)_m/(BFO)_n$ superlattices. In order to investigate the effects of the U_{eff} value on the polarization, the impact of the U_{eff} value on the Fe partial charge change Δq has been investigated for bulk BFO with both G- and C-type AFM states, and the results are plotted [Fig. 9(a)]. It is shown that the Δq increases with the increasing U_{eff} value, i.e., the charge tends to be away from the Fe and localize on its neighboring O ions for both G- and C-type BFO. For G-type BCO, similar trend has been observed. These results suggest that the choice of U_{eff} value affects the exact value of the atomic charge. The variation of polarization for bulk BFO, BCO and $(BCO)_1/(BFO)_1$ superlattices as a function of U_{eff} value are presented [Fig. 9(b)]. It turns out that the choice of U_{eff} value has slight influences on the polarization. This is because the polarization is mainly determined by the charge and displacement of all the ions. Although the U_{eff} value affects the charge of Fe and Cr a lot, it also affects the charge of anions a lot simultaneously, i.e., it is a synergetic effect. On the other hand, the U_{eff} value has small impact on the displacement of all ions. Consequently, the polarization of the materials is affected slightly by the U_{eff} values.

The local polarization can also be described by the local displacement between transition-metal cations and oxygen anions in the superlattices [76]. The local displacement between the Cr/Fe and O ions for the $(BCO)_1/(BFO)_5$ and $(BCO)_5/(BFO)_1$ superlattices along the [001] direction is provided [Fig. 10]. It can be seen that both the displacements of the BFO and BCO part for the $(BCO)_1/(BFO)_5$ and $(BCO)_5/(BFO)_1$ superlattices fluctuate slightly with increasing distance from the

interface, and there is a sharp decrease at the interface, indicative of a sharp change in the polarization at the $BiFeO_3/BiCrO_3$ interface. This polarization discontinuity has been observed in $BiFeO_3/SrTiO_3$ [77], $LaAlO_3/PbTiO_3$ [76], and $PbTiO_3/SrTiO_3$ [78] heterostructures, in which there is an internal electric field and two-dimensional-like electronic gas is formed at the interface. In this study, the polarization discontinuity at the interface and the induced charge reconstruction also contribute to the remarkable reduction in the band gap for the $(BCO)_m/(BFO)_n$ superlattices.

IV. CONCLUSION

In summary, this work provides a systematic DFT+U investigation of $(BCO)_m/(BFO)_1$ and $(BCO)_1/(BFO)_n$ superlattices (m, n=1, 2, 3, 4, 5) to understand how the superlattice structuring and periodicity influence the geometrical structure and electronic properties. Due to the lattice mismatch between BCO and BFO, significant compression of the $BiFeO_3$ layer and large relaxation of the BCO layers along the [001] direction are found for the $(BCO)_m/(BFO)_1$ superlattices, and considerable expansion of the BCO layer and remarkable relaxation of the BFO layers are found for the $(BCO)_1/(BFO)_n$ superlattices. Meanwhile, the octahedral distortion in the $(BCO)_1/(BFO)_n$ superlattices is found to be more significant than that in the $(BCO)_m/(BFO)_1$ superlattices. For all the considered superlattices, the band gap decreases significantly with increasing number of layers of BFO and/or BCO, and the band gap of the $(BCO)_1/(BFO)_n$ superlattices is lower than that of the $(BCO)_m/(BFO)_1$ superlattices for any given value of n and m (n, m>1). Additionally, all the

superlattices retain the direct character of the BFO. Surprisingly, the $(BCO)_m/(BFO)_n$ superlattices show significant band-gap reduction by as much as 1.5 eV. The optimized band gap of 1.6 eV is not only smaller than both BFO and BCO, but also smaller than the alloyed $BiFe_xCr_yO_3$ samples, thus implying good potential for visible-light absorption. The polarization is found to be 92.9-131.0 $\mu C/cm^2$ for the $(BCO)_1/(BFO)_n$ superlattices and 64.8-92.9 $\mu C/cm^2$ for the $(BCO)_m/(BFO)_1$ superlattices, among which the value of 131 $\mu C/cm^2$ for the $(BCO)_1/(BFO)_5$ superlattice is the largest and comparable to the polarization of BFO. These results demonstrate that superlattice ordering can be a new strategy to design low-band-gap semiconductors with fundamental band gaps much smaller than either parent materials, thus opening new perspective for ferroelectric photovaltics.

ACKNOWLEDGEMENTS

H.Y.X was supported by the NSAF Joint Foundation of China (Grant No. U1530129). Z.J. Liu was supported by National Natural Science Foundation of China (Grant No. 11464025), the New Century Excellent Talents in University under Grant no. NCET-11-0906 and the Key Talent Foundation of Gansu Province. L.Q. was supported by National Natural Science Foundation of China (Grant No. 1174044) and the Young 1000-talent Program. D.J.S. was supported by the Department of Energy through the S3TEC Energy Frontier Research Center, award DE-SC0001299. L.W.M. acknowledges the support of the National Science Foundation under grant DMR-1608938.The theoretical calculations were performed using the supercomputer

resources at TianHe-1 located at National Supercomputer Center in Tianjin.

Reference

[1] P. Lopez-Varo, L. Bertoluzzi, J. Bisquert, M. Alexe, M. Coll, J. Huang, J. Antonio Jimenez-Tejada, T. Kirchartz, R. Nechache, F. Rosei, and Y. Yuan, Physical aspects of ferroelectric semiconductors for photovoltaic solar energy conversion, Phys. Rep. **653**, 1, (2016).

[2] S. Y. Yang, L. W. Martin, S. J. Byrnes, T. E. Conry, S. R. Basu, D. Paran, L. Reichertz, J. Ihlefeld, C. Adamo, A. Melville, Y.-H. Chu, C.-H. Yang, J. L. Musfeldt, D. G. Schlom, J. W. A. III, and R. Ramesh, Photovoltaic effects in $BiFeO_3$, Appl. Phys. Lett. **95**, 062909 (2009).

[3] B. Chen, J. Shi, X. Zheng, Y. Zhou, K. Zhu, and S. Priya, Ferroelectric solar cells based on inorganic-organic hybrid perovskites, J. Mater. Chem. A **3**, 7699, (2015).

[4] Y. Liu, S. Wang, Z. Chen, and L. Xiao, Applications of ferroelectrics in photovoltaic devices, Sci. China Mater. **59**, 851, (2016).

[5] C. Paillard, X. Bai, I. C. Infante, M. Guennou, G. Geneste, M. Alexe, J. Kreisel, and B. Dkhil, Photovoltaics with ferroelectrics: current status and beyond, Adv. Mater. **28**, 5153, (2016).

[6] Y. Yuan, Z. Xiao, B. Yang, and J. Huang, Arising applications of ferroelectric materials in photovoltaic devices, J. Mater. Chem. A **2**, 6027, (2014).

[7] S. Y. Yang, J. Seidel, S. J. Byrnes, P. Shafer, C.-H. Yang, M. D. Rossell, P. Yu, Y.-H. Chu, J. F. Scott, J. W. Ager, L. W. Martin, and R. Ramesh, Above-bandgap voltages from ferroelectric photovoltaic devices, Nat. Nanotechnol. **5**, 143, (2010).

[8] V. M. Fridkin, Bulk photovoltaic effect in noncentrosymmetric crystals, Crystallogr. Rep. **46**, 654, (2001).

[9] L. Pintilie, I. Vrejoiu, G. L. Rhun, and M. Alexe, Short-circuit photocurrent in epitaxial lead zirconate-titanate thin films, J. Appl. Phys. **101**, 064109, (2007).

[10] J. Chakrabartty, R. Nechache, S. Li, M. Nicklaus, A. Ruediger, F. Rosei, and D. D. Viehland, Photovoltaic properties of multiferroic $BiFeO_3/BiCrO_3$ heterostructures, ***J. Am. Ceram. Soc. 97, 1837, (2014).***

[11] Y. Li and D. J. Singh, Properties of the ferroelectric visible light absorbing semiconductors: $Sn_2P_2S_6$ and $Sn_2P_2Se_6$, ***Phys. Rev. Mater. 1, 075402, (2017).***

[12] P. Chen, N. J. Podraza, X. S. Xu, A. Melville, E. Vlahos, V. Gopalan, R. Ramesh, D. G. Schlom, and J. L. Musfeldt, Optical properties of quasi-tetragonal $BiFeO_3$ thin films, Appl. Phys. Lett. **96**, 131907, (2010).

[13] K. Y. Yun, D. Ricinschi, T. Kanashima, M. Noda, and M. Okuyama, Giant ferroelectric polarization beyond 150 $\mu C/cm^2$ in $BiFeO_3$ thin film, Jpn. J. Appl. Phys. Part 2-Letters & Express Lett. **43**, L647, (2004).

[14] Y.-H. Chu, L. W. Martin, M. B. Holcomb, and R. Ramesh, Controlling magnetism with multiferroics, Mater. Today **10**, 16, (2007).

[15] C. Ederer and N. A. Spaldin, Effect of epitaxial strain on the spontaneous polarization of thin film ferroelectrics, Phys. Rev. Lett. **95**, 257601, (2005).

[16] S. Gupta, M. Tomar, and V. Gupta, Ferroelectric photovoltaic response to structural transformations in doped $BiFeO_3$ derivative thin films, Mater. Design **105**, 296, (2016).

[17] Y. Sun, X. Liu, J. Zeng, J. Yan, D. Shi, and H. Liu, Photovoltaic effects in polarized polycrystalline $BiFeO_3$ films, J. Electron. Mater. **44**, 4207, (2015).

[18] S. M. Young, F. Zheng, and A. M. Rappe, First-principles calculation of the bulk photovoltaic effect in bismuth ferrite, Phys. Rev. Lett. **109**, 236601, (2012).

[19] P. P. Biswas, T. Chinthakuntla, D. Duraisamy, G. N. Venkatesan, S. Venkatachalam, and P.

Murugavel, Photovoltaic and photo-capacitance effects in ferroelectric $BiFeO_3$ thin film, Appl. Phys. Lett. **110**, 192906, (2017).

[20] M. M. Yang, Z. D. Luo, D. J. Kim, and M. Alexe, Bulk photovoltaic effect in monodomain $BiFeO_3$ thin films, Appl. Phys. Lett. **110**, 183902, (2017).

[21] R. Nechache, C. Harnagea, S. Li, L. Cardenas, W. Huang, J. Chakrabartty, and F. Rosei, Bandgap tuning of multiferroic oxide solar cells, Nat. Photonics. **9**, 61, (2015).

[22] R. Nechache, P. Gupta, C. Harnagea, and A. Pignolet, Enhanced magnetism in epitaxial $BiFeO_3$ / $BiCrO_3$ multiferroic heterostructures, Appl. Phys. Lett. **91**, 222908, (2007).

[23] S. K. Singh, S. Shanthy, and H. Ishiwara, Reduced leakage current in $BiFeO_3$-$BiCrO_3$ nanocomposite films formed by chemical solution deposition, J. Appl. Phys. **108**, 054102 (2010).

[24] S. Gepraegs, M. Opel, S. T. B. Goennenwein, and R. Gross, Multiferroic materials based on artificial thin film heterostructures, Phil. Mag. Lett. **87**, 141, (2007).

[25]P. Couture, G. V. M. Williams, J. Kennedy, J. Leveneur, P. P. Murmu, S. V. Chong, and S. Rubanov, Multiferroic nanocrystalline $BiFeO_3$ and $BiCrO_3$ thin films prepared by ion beam sputtering, Int. J. Nanotechnol. **14**, 56, (2017).

[26] J. W. Kim, C. M. Raghavan, J. W. Kim, and S. S. Kim, Multiferroic properties of a $BiCrO_3$/$BiFeO_3$ double-layered thin film prepared by chemical solution deposition, Ceram. Int. **41**, 7211, (2015).

[27] L. Qiao, S. Zhang, H. Y. Xiao, D. J. Singh, K. H. L. Zhang, Z. J. Liu, X. T. Zu, and S. Li, Orbital controlled band gap engineering of tetragonal $BiFeO_3$ for optoelectronic applications, J. Mater. Chem. C **6**, 1239, (2018).

[28] C. Nie, S. Zhao, Y. Bai, and Q. Lu, The ferroelectric photovoltaic effect of $BiCrO_3$/$BiFeO_3$ bilayer composite films, Ceram. Int. **42**, 14036, (2016).

[29] S. Chakraverty, K. Yoshimatsu, Y. Kozuka, H. Kumigashira, M. Oshima, T. Makino, A. Ohtomo, and M. Kawasaki, Magnetic and electronic properties of ordered double-perovskite La_2VMnO_6 thin films, Phys. Rev. B **84**, 132411, (2011).

[30] S. Chakraverty, A. Ohtomo, D. Okuyama, M. Saito, M. Okude, R. Kumai, T. Arima, Y. Tokura, S. Tsukimoto, Y. Ikuhara, and M. Kawasaki, Ferrimagnetism and spontaneous ordering of transition metals in double perovskite La_2CrFeO_6 films, Phys. Rev. B **84**, 064436, (2011).

[31] M. P. Singh, K. D. Truong, S. Jandl, and P. Fournier, Long-range Ni/Mn structural order in epitaxial double perovskite La_2NiMnO_6 thin films, Phys. Rev. B **79**, 224421, (2009).

[32] K. Ueda, H. Tabata, and T. Kawai, Ferromagnetism in $LaFeO_3$-$LaCrO_3$ superlattices, Science **280**, 1064, (1998).

[33] N. Ichikawa, M. Arai, Y. Imai, K. Hagiwara, H. Sakama, M. Azuma, Y. Shimakawa, M. Takano, Y. Kotaka, M. Yonetani, H. Fujisawa, M. Shimizu, K. Ishikawa, and Y. Cho, Multiferroism at room temperature in $BiFeO_3$/$BiCrO_3$ (111) artificial superlattices, Appl. Phys. Express **1**, 101302, (2008).

[34] G. Kresse and J. Hafner, Ab inito molecular-dynamics for liquid-metals, Phys. Rev. B **47**, 558, (1993).

[35] G. Kresse and J. Furthmiiller, Efficiency of ab-initio total energy calculations for metals and semiconductors using a plane-wave basis set, Comp. Mater. Sci. **6**, 15, (1996).

[36] J. P. Perdew, K. Burke, and M. Ernzerhof, Generalized gradient approximation made simple, Phys. Rev. Lett. **77**, 3865, (1996).

[37] V. I. Anisimov, F. Aryasetiawan, and A. I. Lichtenstein, First-principles calculations of the electronic structure and spectra of strongly correlated systems: the LDA+U method, J.

Phys.-Condens. Mat. **9**, 767, (1997).

[38] H. Dong, C. Chen, S. Wang, W. Duan, and J. Li, Elastic properties of tetragonal $BiFeO_3$ from first-principles calculations, Appl. Phys. Lett. **102**, 182905, (2013).

[39] J. B. Neaton, C. Ederer, U. V. Waghmare, N. A. Spaldin, and K. M. Rabe, First-principles study of spontaneous polarization in multiferroic $BiFeO_3$, Phys. Rev. B **71**, 014113, (2005).

[40] D. Ricinschi, K. Y. Yun, and M. Okuyama, A mechanism for the 150 $\mu C/cm^{-2}$ polarization of $BiFeO_3$ films based on first-principles calculations and new structural data, J. Phys.-Condens. Mat. **18**, L97, (2006).

[41] O. Dieguez, O. E. Gonzalez-Vazquez, J. C. Wojdel, and J. Iniguez, First-principles predictions of low-energy phases of multiferroic $BiFeO_3$, Phys. Rev. B **83**, 094105, (2011).

[42] N. Feng, W. Mi, X. Wang, Y. Cheng, and U. Schwingenschlogl, Superior properties of energetically stable $La_{2/3}Sr_{1/3}MnO_3$/tetragonal $BiFeO_3$ multiferroic superlattices, ACS Appl. Mater. Inter. **7**, 10612, (2015).

[43] T. P. Comyn, T. Stevenson, M. Al-Jawad, S. L. Turner, R. I. Smith, A. J. Bell, and R. Cywinski, High temperature neutron diffraction studies of $0.9BiFeO_3$-$0.1PbTiO_3$, J. Appl. Phys. **105**, 094108, (2009).

[44] H. L. Liu, M. K. Lin, Y. R. Cai, C. K. Tung, and Y. H. Chu, Strain modulated optical properties in $BiFeO_3$ thin films, Appl. Phys. Lett. **103**, 181907, (2013).

[45] C. Himcinschi, A. Bhatnagar, A. Talkenberger, M. Barchuk, D. R. T. Zahn, D. Rafaja, J. Kortus, and M. Alexe, Optical properties of epitaxial BiFeO3 thin films grown on LaAlO3, Appl. Phys. Lett. **106**, (2015).

[46] S. Mamoun, A. E. Merad, and L. Guilbert, Energy band gap and optical properties of lithium niobate from ab initio calculations, Comp. Mater. Sci. **79**, 125, (2013).

[47] S. Froyen, D. M. Wood, and A. Zunger, Structural and electronic properties of epitaxial thin-layer Si_nGe_n superlattices, Phys. Rev. B **37**, 6893, (1988).

[48] D. H. Kim, H. N. Lee, M. Varela, and H. M. Christen, Antiferroelectricity in multiferroic $BiCrO_3$ epitaxial films, Appl. Phys. Lett. **89**, 162904, (2006).

[49] T. Qi, I. Grinberg, and A. M. Rappe, Correlations between tetragonality, polarization, and ionic displacement in $PbTiO_3$-derived ferroelectric perovskite solid solutions, Phys. Rev. B **82**, 134113, (2010).

[50] M. P. K. Sahoo, Y. Zhang, and J. Wang, Enhancement of ferroelectric polarization in layered $BaZrO_3$/$BaTiO_3$ superlattices, Phys. Lett. A **380**, 299, (2016).

[51] C. Zuo, S. Lu, X. Zhou, and Y. Zhang, Dependence of the structures and properties on $LaAlO_3$ cap layer in $LaAlO_3$/$BaTiO_3$ superlattices, Appl. Phys. Lett. **92**, 012913, (2008).

[52] T. Choi and J. Lee, Structural and dielectric properties of artificial $PbZrO_3$/$PbTiO_3$ superlattices grown by pulsed laser deposition, Thin Solid Films **475**, 283, (2005).

[53] H. M. Christen, E. D. Specht, S. S. Silliman, and K. S. Harshavardhan, Ferroelectric and antiferroelectric coupling in superlattices of paraelectric perovskites at room temperature, Phys. Rev. B **68**, 020101, (2003).

[54] R. J. Zeches, M. D. Rossell, J. X. Zhang, A. J. Hatt, Q. He, C. H. Yang, A. Kumar, C. H. Wang, A. Melville, C. Adamo, G. Sheng, Y. H. Chu, J. F. Ihlefeld, R. Erni, C. Ederer, V. Gopalan, L. Q. Chen, D. G. Schlom, N. A. Spaldin, L. W. Martin, and R. Ramesh, A strain-driven morphotropic phase boundary in $BiFeO_3$, Science **326**, 977, (2009).

[55] M. D. Rossell, R. Erni, M. P. Prange, J. C. Idrobo, W. Luo, R. J. Zeches, S. T. Pantelides, and R.

Ramesh, Atomic structure of highly strained $BiFeO_3$ thin films, Phys. Rev. Lett. **108**, 047601, (2012).

[56] H. Bea, B. Dupe, S. Fusil, R. Mattana, E. Jacquet, B. Warot-Fonrose, F. Wilhelm, A. Rogalev, S. Petit, V. Cros, A. Anane, F. Petroff, K. Bouzehouane, G. Geneste, B. Dkhil, S. Lisenkov, I. Ponomareva, L. Bellaiche, M. Bibes, and A. Barthelemy, Evidence for room-temperature multiferroicity in a compound with a giant axial ratio, Phys. Rev. Lett. **102**, 217603, (2009).

[57] J. X. Zhang, Q. He, M. Trassin, W. Luo, D. Yi, M. D. Rossell, P. Yu, L. You, C. H. Wang, C. Y. Kuo, J. T. Heron, Z. Hu, R. J. Zeches, H. J. Lin, A. Tanaka, C. T. Chen, L. H. Tjeng, Y. H. Chu, and R. Ramesh, Microscopic origin of the giant ferroelectric polarization in tetragonal-like $BiFeO_3$, Phys. Rev. Lett. **107**, 147602, (2011).

[58] ***M. Lannoo and M. Schluter***, Calculation of the Kohn-Sham potential and its discontinuity for a model-semiconductor, Phys. Rev. B **32**, 3890, (1985).

[59] L. Makinistian and E. A. Albanesi, Ab initio calculations of the electronic and optical properties of germanium selenide, J. Phys.-Condens. Mat. **19**, 186211, (2007).

[60]M. G. Brik, First-principles study of the electronic and optical properties of $CuXS_2$ (X = Al, Ga, In) and $AgGaS_2$ ternary compounds, J. Phys.-Condens. Mat. **21**, 485502, (2009).

[61] A. O'Hara, T. N. Nunley, A. B. Posadas, S. Zollner, and A. A. Demkov, Electronic and optical properties of NbO_2, J. Appl. Phys. **116**, 213705, (2014).

[62] A. Hussain Reshak, S. Auluck, and I. V. Kityk, Specific features in the band structure and linear and nonlinear optical susceptibilities of $La_2CaB_{10}O_{19}$ crystals, Phys. Rev. B **75**, 245120, (2007).

[63] H. J. Feng, K. Yang, W. Deng, M. M. Li, M. Z. Wang, B. Duan, F. Liu, J. S. Tian, and X. H. Guo, The origin of enhanced optical absorption of the $BiFeO_3$/ZnO heterojunction in the visible and terahertz regions, Phys. Chem. Chem. Phys. **17**, 26930, (2015).

[64] F. Tran and P. Blaha, Accurate band gaps of semiconductors and insulators with a semilocal exchange-correlation potential, Phys. Rev. Lett. **102**, 226401, (2009).

[65] M. R. Boufatah and A. E. Merad, Structural stability, elastic and electronic properties of zincblende $(GaN)_1/(ZnO)_1$ superlattice: Modified Becke-Johnson exchange potential, Mat. Sci. Semicon. Proc. **19**, 179, (2014).

[66] X. Y. Cui, B. Delley, and C. Stampfl, Band gap engineering of wurtzite and zinc-blende GaN/AlN superlattices from first principles, J. Appl. Phys. **108**, 103701, (2010).

[67] E. Bailon-Garcia, A. Elmouwahidi, F. Carrasco-Marin, A. F. Perez-Cadenas, and F. J. Maldonado-Hodar, Development of Carbon-ZrO_2 composites with high performance as visible-light photocatalysts, Appl. Catal. B-Environ. **217**, 540, (2017).

[68] S. A. Rawool, M. R. Pai, A. M. Banerjee, A. Arya, R. S. Ningthoujam, R. Tewari, R. Rao, B. Chalke, P. Ayyub, A. K. Tripathi, and S. R. Bharadwaj, *pn* Heterojunctions in NiO:TiO_2 composites with type-II band alignment assisting sunlight driven photocatalytic H_2 generation, Appl. Catal. B-Environ. **221**, 443, (2018).

[69] Y. Wang, K. Lopata, S. A. Chambers, N. Govind, and P. V. Sushko, Optical absorption and band gap reduction in $(Fe_{1-x}Cr_x)_2O_3$ solid solutions: a first-principles study, J. Phys. Chem. C **117**, 25504, (2013).

[70] H. Mashiko, T. Oshima, and A. Ohtomo, Band-gap narrowing in alpha-$(Cr_xFe_{1-x})_2O_3$ solid-solution films, Appl. Phys. Lett. **99**, 241904, (2011).

[71] S. E. Chamberlin, Y. Wang, K. Lopata, T. C. Kaspar, A. W. Cohn, D. R. Gamelin, N. Govind, P. V. Sushko, and S. A. Chambers, Optical absorption and spectral photoconductivity in

alpha-$(Fe_{1-x}Cr_x)_2O_3$ solid-solution thin films, J. Phys.-Condens. Mat. **25**, 392002, (2013).

[72] C. Himcinschi, I. Vrejoiu, M. Friedrich, E. Nikulina, L. Ding, C. Cobet, N. Esser, M. Alexe, D. Rafaja, and D. R. T. Zahn, Substrate influence on the optical and structural properties of pulsed laser deposited $BiFeO_3$ epitaxial films, J. Appl. Phys. **107**, 123524, (2010).

[73] D. Sando, C. Carretero, M. N. Grisolia, A. Barthelemy, V. Nagarajan, and M. Bibes, Revisiting the optical band gap in epitaxial $BiFeO_3$ thin films, Adv. Opt. Mater. **6**, 1700836, (2018).

[74] H. Matsuo, Y. Kitanaka, R. Inoue, Y. Noguchi, and M. Miyayama, Heavy Mn-doping effect on spontaneous polarization in ferroelectric $BiFeO_3$ thin films, Jpn. J. Appl. Phys. **54**, 10NA03, (2015).

[75] D. Ricinschi, K. Y. Yun, and M. Okuyama, First-principles study of $BiFeO_3$ films with giant polarization and its dependence on structural parameters, Ferroelectrics **335**, 181, (2006).

[76] P. X. Zhou, S. Dong, H. M. Liu, C. Y. Ma, Z. B. Yan, C. G. Zhong, and J. M. Liu, Ferroelectricity driven magnetism at domain walls in $LaAlO_3/PbTiO_3$ superlattices, Sci. Rep. **5**, 13052, (2015).

[77] Z. Zhang, P. Wu, L. Chen, and J. Wang, First-principles prediction of a two dimensional electron gas at the $BiFeO_3/SrTiO_3$ interface, Appl. Phys. Lett. **99**, 062902, (2011).

[78] L. Y. Wei, C. Lian, and S. Meng, Prediction of two-dimensional electron gas mediated magnetoelectric coupling at ferroelectric $PbTiO_3/SrTiO_3$ heterostructures, Phys. Rev. B **95**, 184102, (2017).

Table 1. The structural parameters and band gap (E_g) of BFO and BCO with G-type and C-type AFM spin states. $\angle O_A$-M-O_B: bond angle (M= Fe or Cr); MM: magnetic moment of Fe and Cr.

Compounds		*a* (Å)	*c* (Å)	*c*/*a*	$\angle O_A$-M-O_B (°)	E_g (eV)	MM (μ_B)
BFO	G-type AFM	3.755	4.879	1.300	110.7	1.62	4.136
	C-type AFM	3.753	4.890	1.303	110.9	1.71	4.130
	Exp.[a,b,c]	3.72	4.67	1.255		3.1	4.34
	Other cal.[d]					1.90	4.18
BCO	G-type AFM	3.926	4.073	1.037	96.6	0.94	2.944
	C-type AFM	3.921	4.087	1.042	96.7	0.69	2.923
	Exp.[e,f]	3.889	3.902	1.003		2.37	

[a]Ref. 40; [b]Ref. 44; [c]Ref. 43; [d]Ref. 42; [e]Ref. 28; [f]Ref. 50.

Table 2. The calculated lattice parameters (the values of *c* and *c/a* are the average values of overall superlattices), average interlayer distance Δ*d* and bond angles of BFO, BCO and $(BCO)_m/(BFO)_n$ superlattices.

Compounds	*a*(Å)	*c*(Å)	*c*/*a*	Δd_{BFO} (Å)	Δd_{BCO} (Å)	$\angle O_A\text{-Cr-}O_B$ (°)	$\angle O_A\text{-Fe-}O_B$ (°)
BFO	3.755	4.879	1.300	4.879	-	-	110.7
BCO	3.926	4.073	1.037		4.073	96.6	-
$(BCO)_1/(BFO)_1$	3.856	4.392	1.139	4.456	4.327	100.7	105.0
$(BCO)_2/(BFO)_1$	3.905	4.175	1.069	4.243	4.141	97.91	101.1
$(BCO)_3/(BFO)_1$	3.914	4.134	1.056	4.203	4.112	97.4	100.2
$(BCO)_4/(BFO)_1$	3.917	4.117	1.051	4.183	4.101	97.2	99.8
$(BCO)_5/(BFO)_1$	3.920	4.106	1.047	4.166	4.094	97.0	99.5
$(BCO)_1/(BFO)_2$	3.802	4.660	1.226	4.701	4.578	104.8	108.3
$(BCO)_1/(BFO)_3$	3.784	4.744	1.254	4.764	4.680	106.1	109.2
$(BCO)_1/(BFO)_4$	3.776	4.775	1.264	4.790	4.741	106.6	109.5
$(BCO)_1/(BFO)_5$	3.772	4.798	1.272	4.808	4.751	107.1	109.8

Table 3. The calculated formation energies for $(BCO)_m/(BFO)_n$ superlattices.

Superlattices	Formation energy (eV)
$(BCO)_1/(BFO)_1$	1.94
$(BCO)_2/(BFO)_1$	2.36
$(BCO)_3/(BFO)_1$	2.46
$(BCO)_4/(BFO)_1$	2.50
$(BCO)_5/(BFO)_1$	2.51
$(BCO)_1/(BFO)_2$	2.50
$(BCO)_1/(BFO)_3$	2.70
$(BCO)_1/(BFO)_4$	2.81
$(BCO)_1/(BFO)_5$	2.86

Table 4. A comparison of the band gap (eV) for BFO, BCO and $(BCO)_m/(BFO)_1$ (m=1 to 5) superlattices obtained from DFT, DFT with scissor correction and DFT/meta-GGA-mBJ calculations.

	DFT	DFT with scissor correction	DFT/meta-GGA -mBJ	Exp.
BFO	1.62	3.1	2.92	3.1[a,b]
BCO	0.94	2.42	2.27	2.37[c]
$(BCO)_1/(BFO)_1$	0.48	1.96	2.03	
$(BCO)_2/(BFO)_1$	0.33	1.81	1.84	
$(BCO)_3/(BFO)_1$	0.27	1.75	1.77	
$(BCO)_4/(BFO)_1$	0.18	1.66	1.69	
$(BCO)_5/(BFO)_1$	0.21	1.69	1.71	

[a]Ref. 44; [b]Ref.45; [c]Ref. 28.

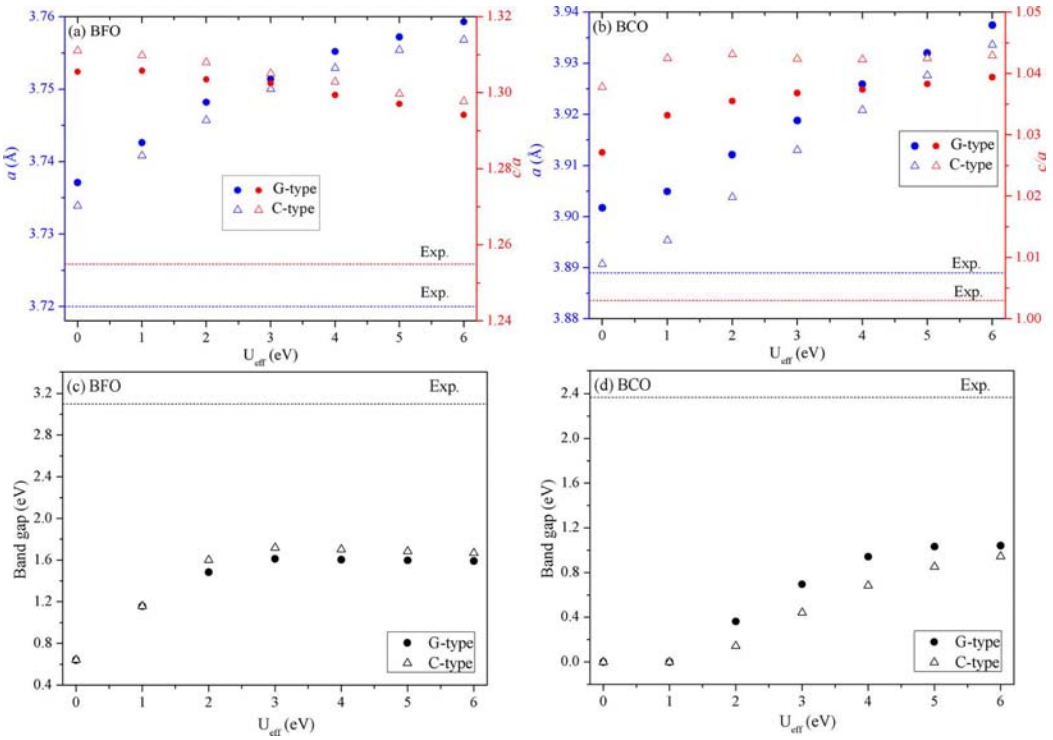

Figure 1. Variation of lattice parameter *a* (lattice constants *a* in blue and *c/a* ratio in red) for (a) G- and C-type BFO and (b) G- and C-type BCO as a function of U_{eff} value, and variation of band gap for (c) G- and C-type BFO and (d) G- and C-type BCO as a function of U_{eff} value. The dash lines are the experimental results.

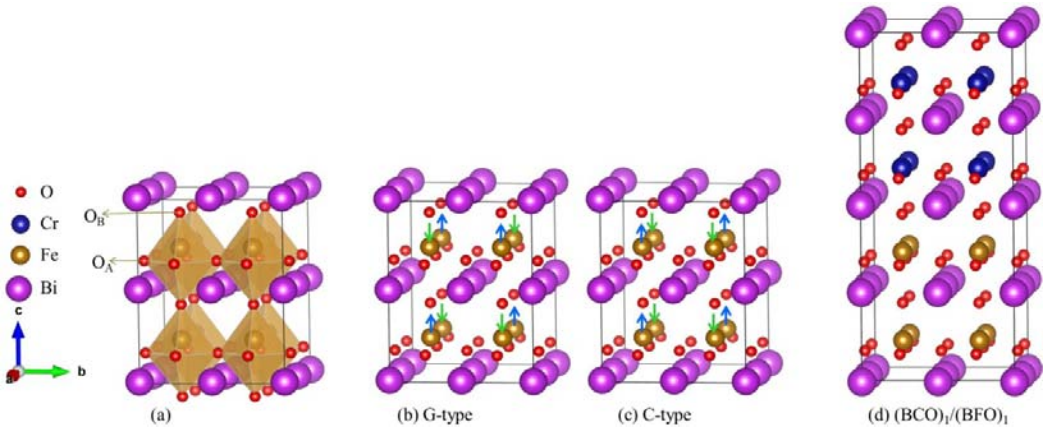

Figure 2. Schematic view of (a) 2×2×2 supercell for BFO; (b) BFO with a G-type AFM state; (c) BFO with a C-type AFM state and (d) optimized $(BCO)_1/(BFO)_1$ superlattice.

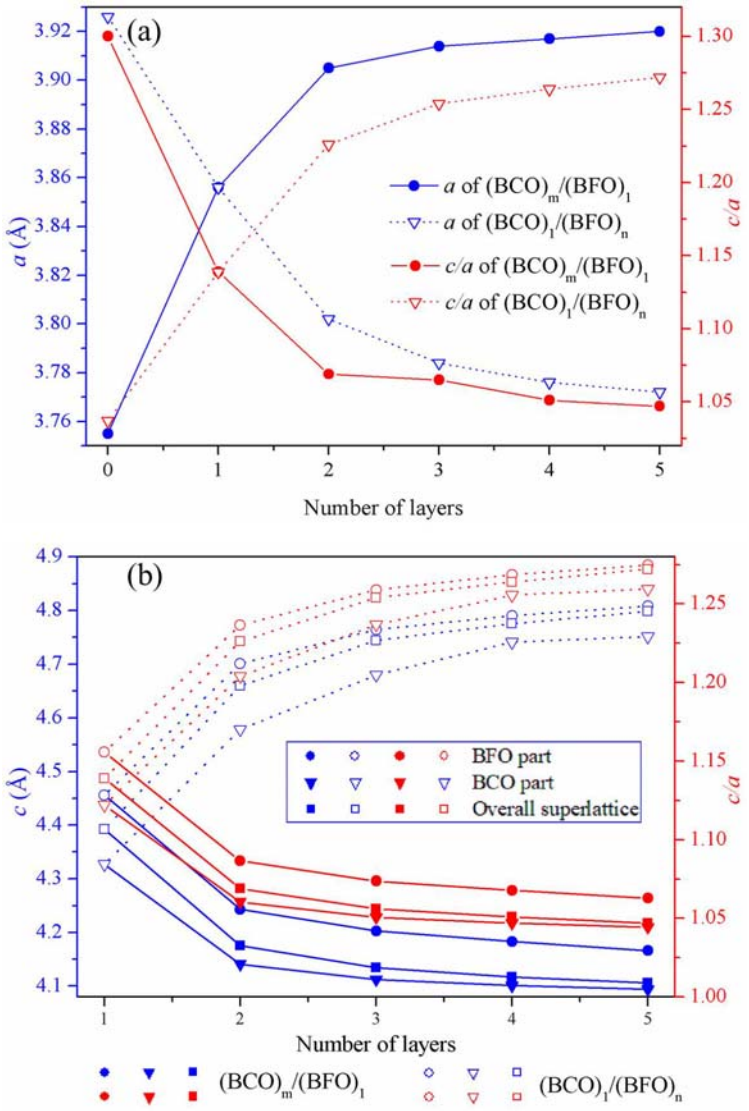

Figure 3. (a) Variation of lattice constants *a* (blue) and *c/a* (red) for $(BCO)_m/(BFO)_1$ and $(BCO)_1/(BFO)_n$ (m, n = 0, 1, 2, 3, 4, 5) as a function of number of layers; (b) variation of out-of-plane lattice constants *c* (blue) and *c/a* (red) for $(BCO)_m/(BFO)_1$ (solid) and $(BCO)_1/(BFO)_n$ (hollow) (m, n = 0, 1, 2, 3, 4, 5) as a function of number of layers. The circle sign is the average of BFO part in superlattice, the triangle down sign is the average of BCO part in superlattice and the square sign is the average of overall superlattices.

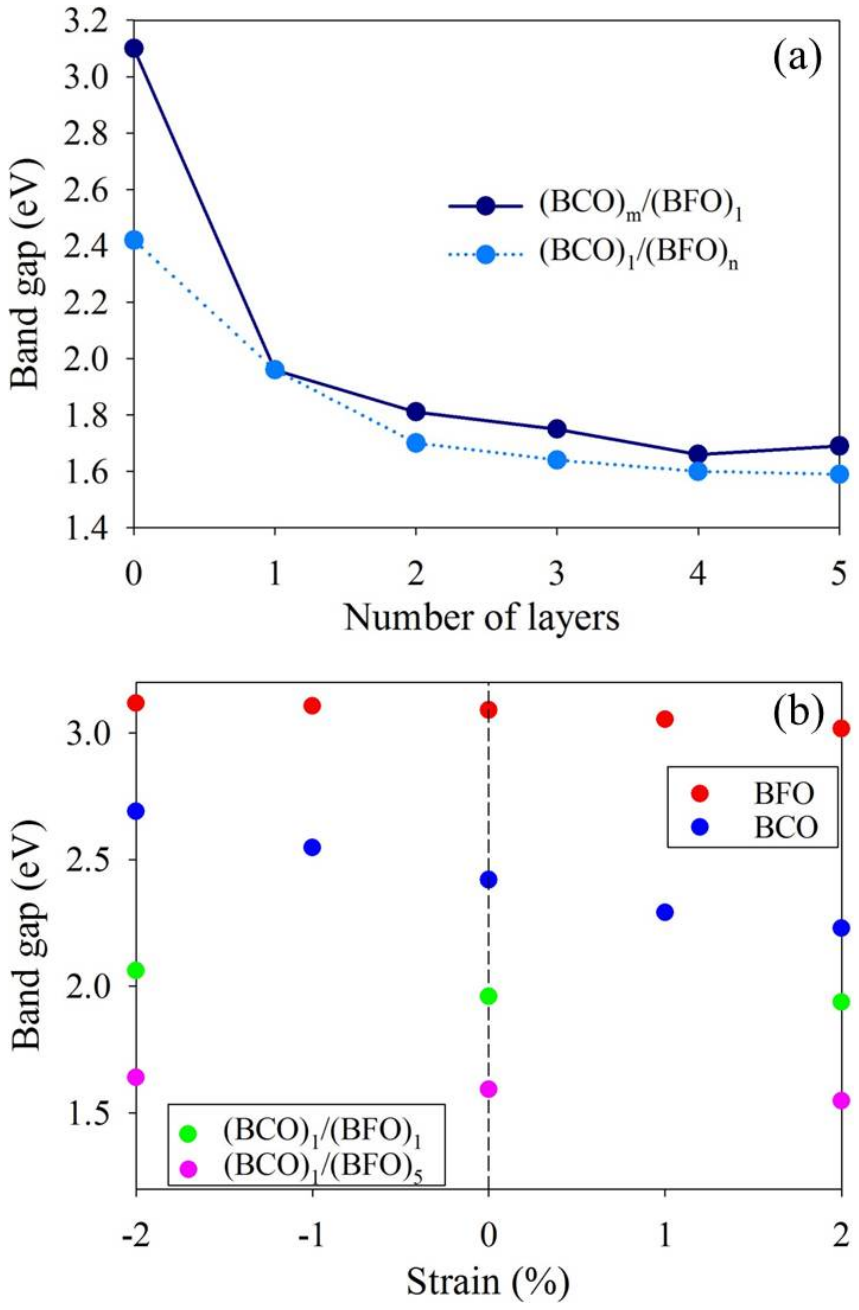

Figure 4. (a) Variation of band gap for $(BCO)_m/(BFO)_1$ and $(BCO)_1/(BFO)_n$ (m, n = 1, 2, 3, 4, 5) as a function of number of layers; (b) variation of band gap for bulk BFO and BCO as a function of strain. The negative values indicate compressive strain and the positive values indicate tensile strain.

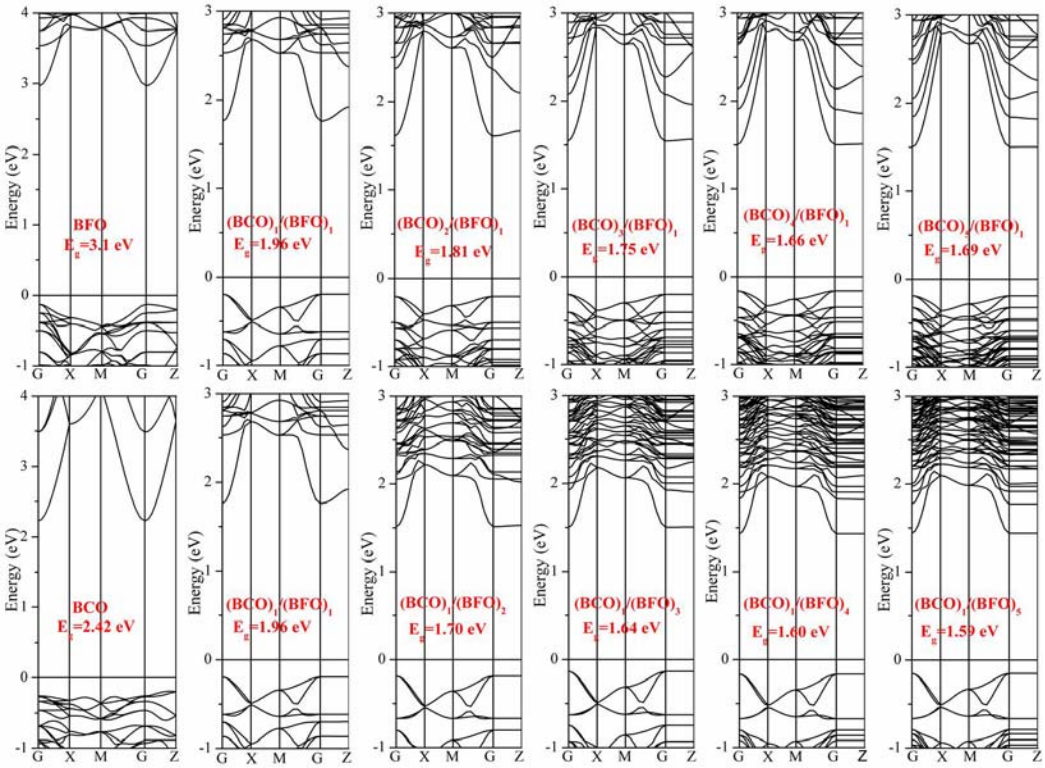

Figure 5. Band structure of bulk BFO, BCO, $(BCO)_m/(BFO)_1$ and $(BCO)_1/(BFO)_n$ (m, n =1, 2, 3, 4, 5) superlattices. The Fermi level is located at 0 eV.

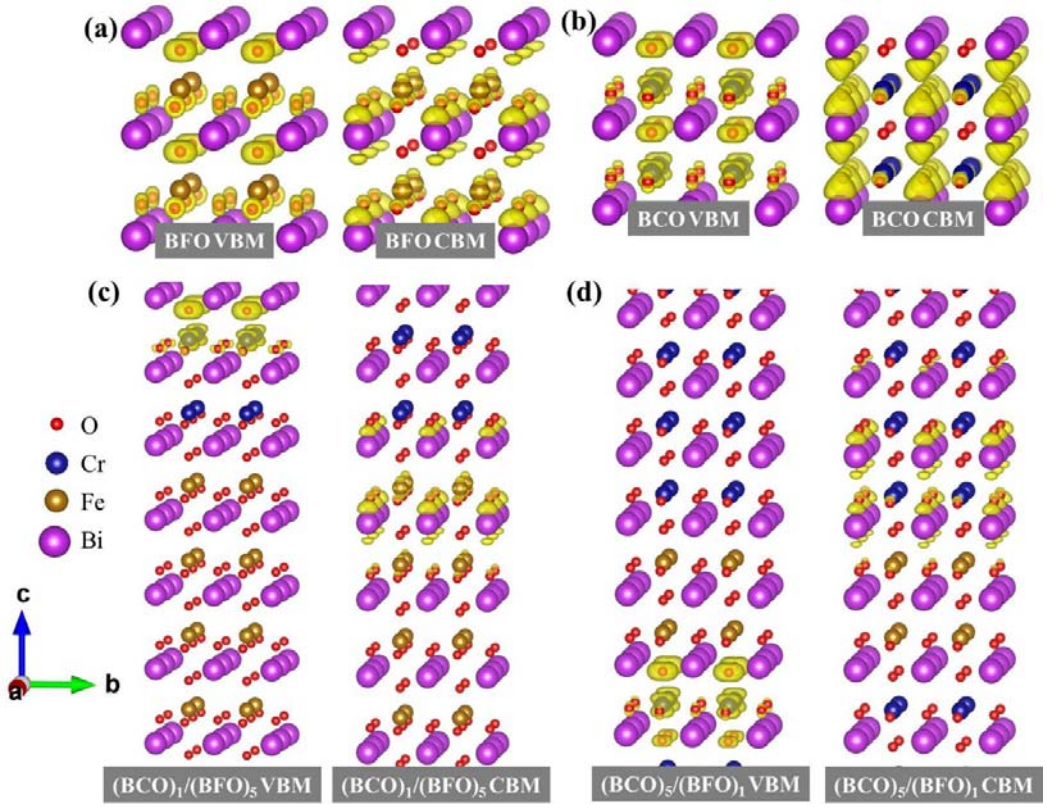

Figure 6. Partial charge density distributions at VBM (left) and CBM (right) for (a) BFO; (b) BCO; (c) $(BCO)_1/(BFO)_5$ and (d) $(BCO)_5/(BFO)_1$.

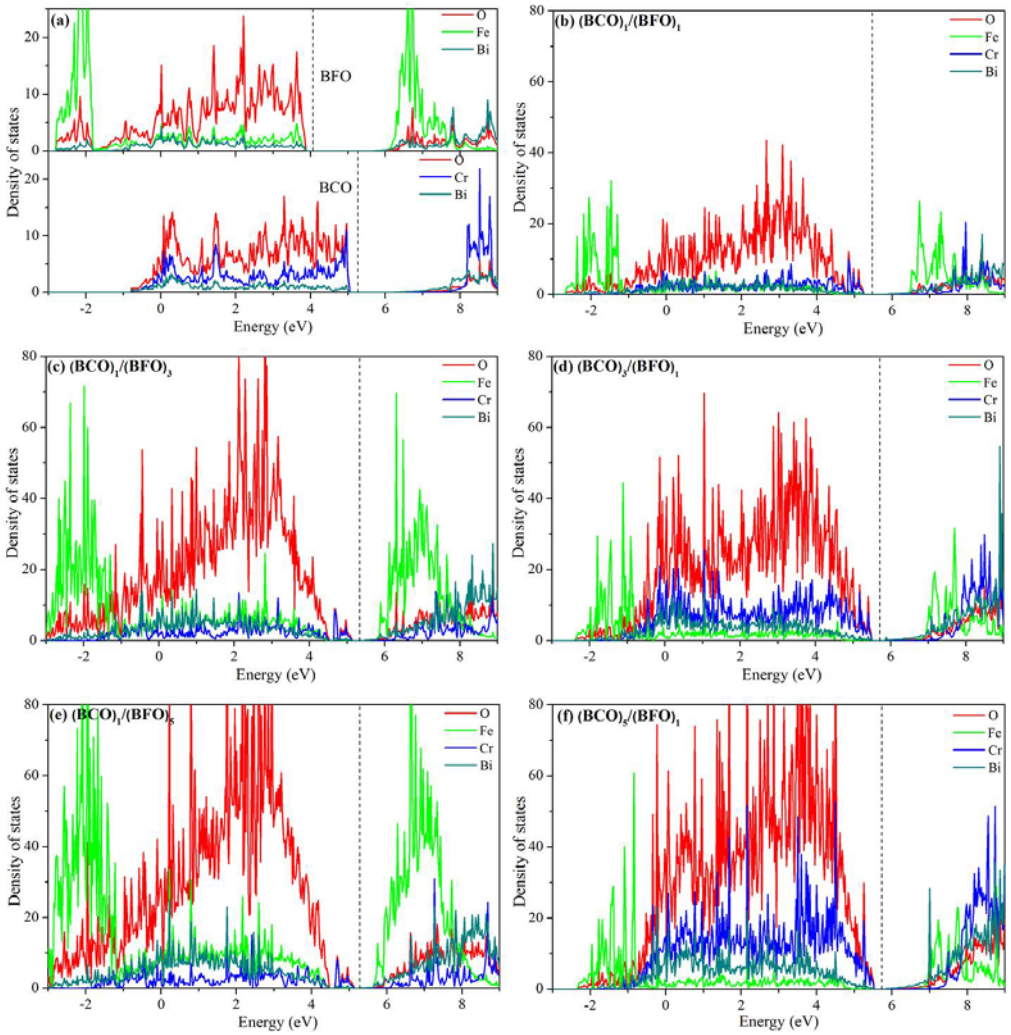

Figure 7. Atomic projected density of state distribution for (a) parents materials (up: BFO; down: BCO); (b) $(BCO)_1/(BFO)_1$; (c) $(BCO)_1/(BFO)_3$; (d) $(BCO)_3/(BFO)_1$; (e) $(BCO)_1/(BFO)_5$ and (f) $(BCO)_5/(BFO)_1$. The Fermi level is indicated by the dashed line.

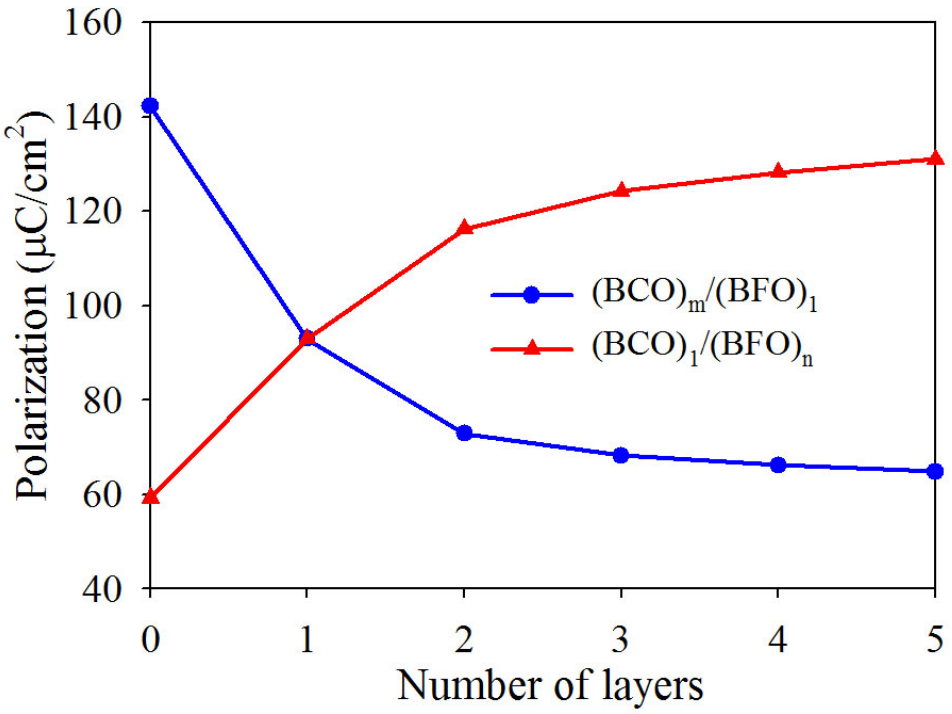

Figure 8. Variation of polarization for $(BCO)_m/(BFO)_1$ and $(BCO)_1/(BFO)_n$ (m, n = 0, 1, 2, 3, 4, 5) as a function of number of layers.

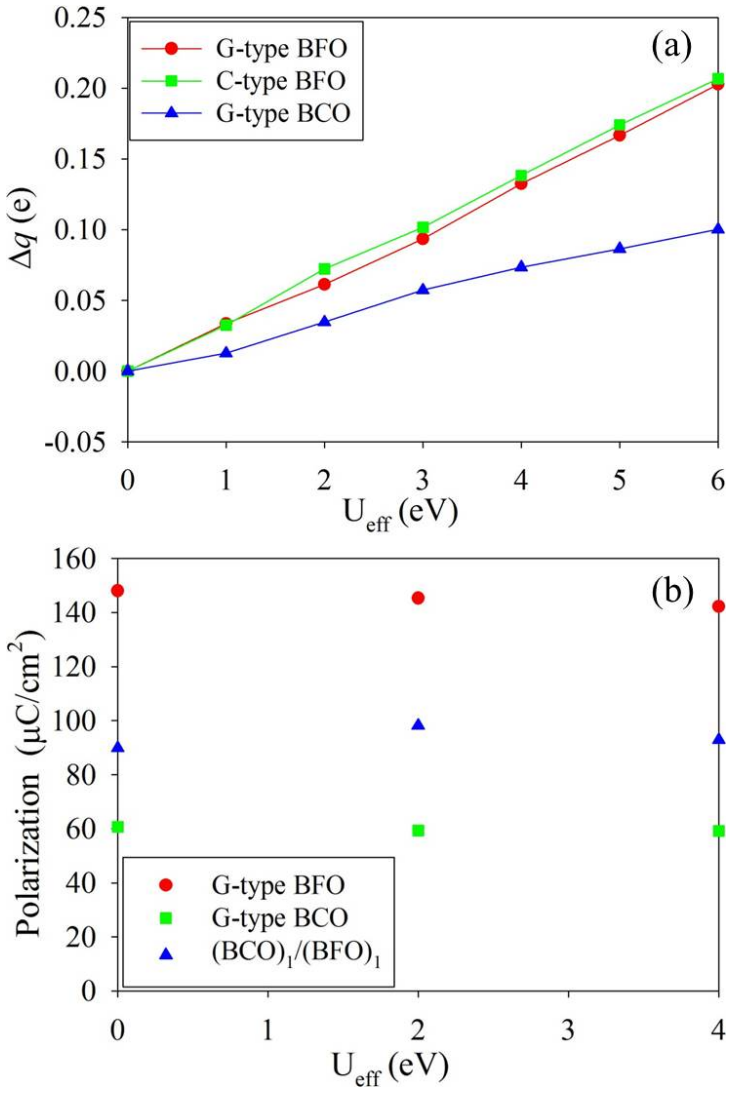

Figure 9. (a) Variation of TM partial charge Δq with U_{eff} value for bulk BFO and BCO. The TM are Fe and Cr in the BFO and BCO, respectively; (b) variation of polarization for bulk BFO, BCO and $(BCO)_1/(BFO)_1$ superlattices as a function of U_{eff} value.

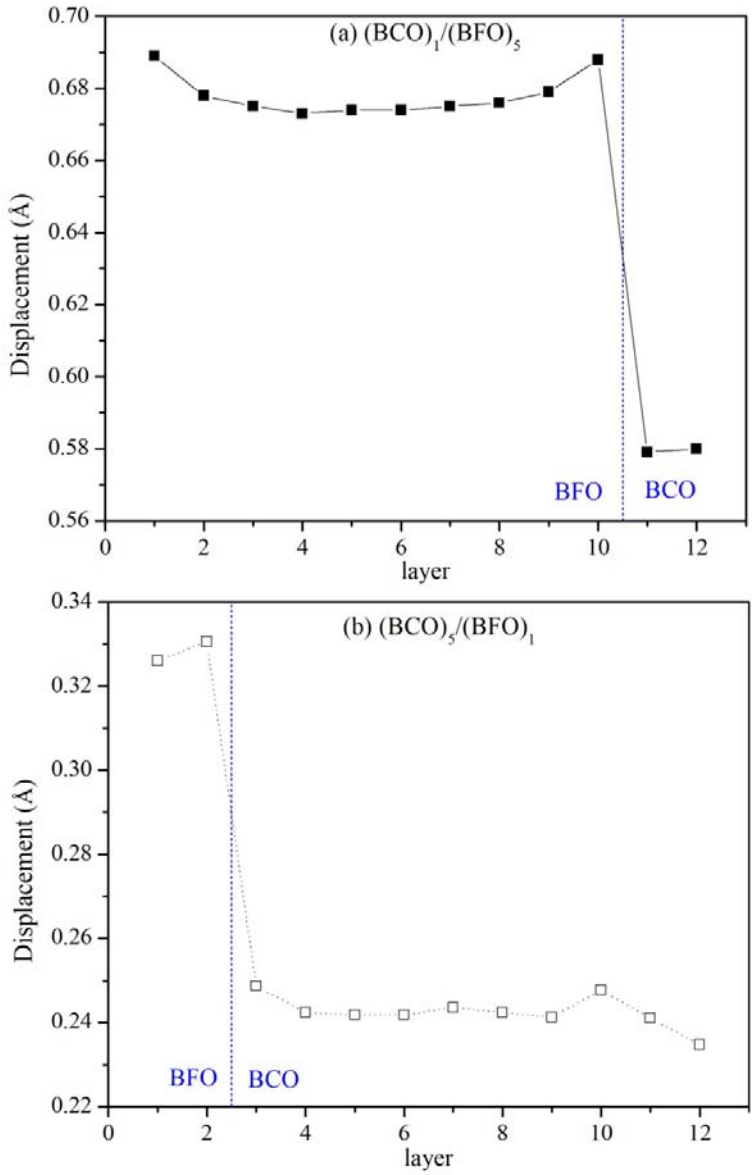

Figure 10. Local displacement between Fe/Cr ions and O ions for (a) $(BCO)_1/(BFO)_5$ and (b) $(BCO)_5/(BFO)_1$ superlattices.